electronics

MDPI

Article

Closed Loop Control of a Series Class-E Voltage-Clamped Resonant Converter for LED Supply with Dimming Capability

Javier Ribas *, Pablo J. Quintana, Jesus Cardesin, Antonio J. Calleja and Juan M. Lopera

CE3I2 Group, Department of Electrical Engineering, University of Oviedo, 33204 Gijon, Spain; quintanapablo@uniovi.es (P.J.Q.); cardesin@uniovi.es (J.C.); calleja@uniovi.es (A.J.C.); lopera@uniovi.es (J.M.L.)

* Correspondence: ribas@uniovi.es; Tel.: +34-985-182-550

Received: 30 September 2019; Accepted: 19 November 2019; Published: 21 November 2019

Abstract: In this work, a new closed-loop control system is applied to a class-E resonant DC–DC converter with voltage clamp used for light-emitting diode (LED) supply. The proposed power topology was first described by Ribas et al. in a recent work. In the present paper, the LED current is sensed and used to implement a feedback control loop instead of the simplified feedforward scheme used in this previous reference. To design the control, a novel, simplified small-signal model is presented. This model is used to analyze the converter behavior as a function of the output power. The proposed approximation is significantly simpler than the multifrequency averaging technique normally used to analyze resonant converters. The feedback control loop is designed to reduce the LED low frequency current ripple while providing dimming control. Both the model and the control are verified by simulation and laboratory experimentation and the results obtained are in good accordance with the expected values.

Keywords: light-emitting diode (LED) driver; high efficiency LEDs; resonant DC–DC converter; Class-E inverter; single-switch topology; voltage clamp; small-signal dynamic model; closed-loop control

1. Introduction

This work is a continuation of the one published in Reference [1].

The use of systems that automatically adapt the lighting level to the actual illumination conditions allows for significant energy savings [2,3]. In this type of system, occupancy- and light-level sensors can be used to automatically deactivate artificial lighting where it is not needed or maintain the desired level of light by adjusting the electricity consumption based on the available natural light. In this context, light-emitting diode (LED) lamps are especially suitable due to their instantaneous turn-on, reduced in-rush current, ease of level regulation and the fact that their useful life is not affected by the number of on–off cycles or frequent operation at low power levels [4,5]. These features, combined with the possibility of using cost-effective embedded control systems inside every luminaire, allows LED lamps to be controlled using a dimming protocol as part of a networked lighting system. Embedded software on microcontrollers further enables adding a first layer of intelligence to LED lighting systems. In these lighting systems, complex control strategies can be used to maximize user comfort while minimizing power consumption [6–8].

There are two basic techniques to control the light produced by a LED lamp: constant current reduction (CCR) and pulse-width-modulation (PWM). In CCR dimming, the LED current is adjusted between nominal and a minimum value using a constant current. The main drawback of this technique is due to the dependence of the correlated-color-temperature (CCT) with the driving current that most

white LEDs have [9,10]. Therefore, CCR dimming should be avoided in applications where color consistency is critical. PWM dimming is based on alternating between nominal and zero current at a frequency above 1.25 kHz. In this technique, the output power is controlled by changing the ratio between the on time and the period. The CCT shift that occurs with CCR dimming is avoided with this control strategy. The 1.25 kHz limit is set by the standard IEEE PAR1789 [11] to mitigate the adverse effects that the 100% light ripple provided by the PWM control has over the final user. In fact, using a PWM frequency above 3 kHz is recommended. In any case, this technique must be avoided in environments with fast moving objects, as it might produce annoying visual artifacts [12].

In this work, a CCR dimming technique is proposed to control the LED current using the resonant series-regulator introduced in [1]. This topology is especially suited to work as a post-regulator in a two-stage LED drive supplied from the alternating current (AC) mains. Two-stage topologies are the preferred solution of most ballast manufacturers in order to comply with the harmonic standard regulations, provide dimming control and minimize light output flicker [13–16]. The first stage provides power-factor correction and the second stage works as a direct current (DC)–DC post-regulator for LED current control. In Reference [1], authors introduced a novel resonant converter derived from a Class-E inverter. In this prior work, authors described the circuit operation, provided a simplified procedure for circuit design and used the results to build and test an experimental prototype with dimming control. However, the proposed control was based on a feedforward scheme and no actual current feedback was implemented. However, this kind of control may lead to important variations in the operating point due to tolerances and deviations in component values caused by temperature effects, aging, etc. In present work, a new closed-loop control scheme for the topology proposed in Reference [1] will be presented (see Figure 1). To do so, the LED current will be measured indirectly from the source current (i_B) using a low-cost nonisolated sensing circuit. This current will then be used to implement a feedback loop and automatically adjust the frequency according to the desired LED current reference. Similar closed loop strategies for CCR dimming are described in prior literature for other circuit configurations [17–19]. However, as this is a totally different power topology, both the modeling and the practical implementation of the current sensing circuit are original contributions of this work.

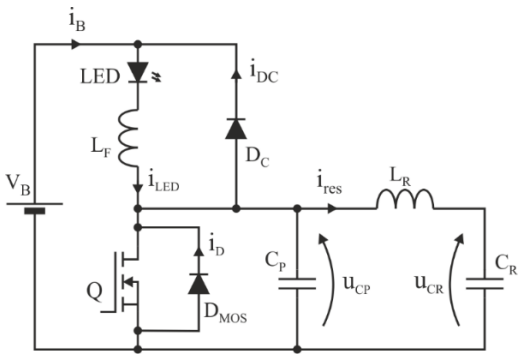

Figure 1. Schematic of the proposed circuit.

A brief revision of the static characteristics obtained in [1] is the first step towards the analysis of the circuit. These characteristics were intended for the converter design at nominal operating conditions. In this work, this study will be modified and oriented to determine how the operating point changes depending on the dimming level. This analysis is required to determine how the stresses are modified and also to check if the soft-switching condition is maintained across the desired dimming range.

In Reference [1], a sensitivity analysis was carried out to determine the gain of the feedforward control required to compensate for deviations in both the bus and LED voltages. It was demonstrated that both effects could be approximately compensated using a single voltage measurement. In present work, this sensitivity analysis will be used as the starting point to obtain an approximated small signal

dynamic model whose parameters change according to the dimming level. This simplified model will be used to calculate the transfer function of the controller required to meet the low-frequency ripple requirements of the IEEE PAR1789 [11] and ensure stable operation across the entire dimming range.

The most commonly used technique to analyze the dynamic behavior of a resonant converter is the Multifrequency Averaging (MFA) technique [20–22]. This method is used when the high frequency current ripple in the converter inductors or the voltage ripple in the capacitors are too high to be neglected as they are in the traditional averaging procedure [23]. MFA is based on applying the Fourier transform on the converter's signals inside a sliding window whose length is equal to the switching period. This analysis allows obtaining the dynamic evolution of the DC and some selected harmonics. Normally, for resonant converters, the MFA analysis is applied only to the DC and fundamental components and higher order harmonics are neglected. Typically, the nonlinear elements of the circuit are analyzed using the describing function [21]. This procedure provides a fairly complicated model where in most cases, obtaining the converter transfer function cannot be made in a straightforward way.

In the proposed circuit, the filter inductor L_F is used to provide a constant LED current with a negligible ripple. Therefore, the dynamics associated with this inductor will be much slower compared with the components of the resonant tank (L_R, C_R and C_P). The approximation that will be used in this work consists in considering that solely L_F determines the dynamics of the LED current and all other dynamic effects can be considered instantaneous in comparison. This approximation leads to a first-order model that is extremely simple to use.

The remainder of the paper will be organized as follows. In the first section, the basic circuit behavior will be briefly explained. In the third section, the static analysis of the circuit will be revised paying special attention to how the circuit behaves when the power level is reduced below its nominal value. The basic design equations and charts will also be revised and summarized in this section. A more detailed explanation can be found in Reference [1]. The fourth section of the paper will be dedicated to revise the small-signal static analysis and to introduce a novel simplified dynamic model of proposed converter. This model will be used in Section 5 to design a proportional-integral (PI) controller. The design methodology will be summarized in this section. The simulation and experimental results will be presented in Sections 6 and 7 respectively. In the final section, the conclusions of this work will be presented.

2. Simplified Analysis of the Circuit Operation

Figure 2 shows the basic waveforms of the proposed circuit. To simplify the analysis, the resonant current i_{res} will be approximated as a pure sinusoidal waveform and the high-frequency current ripple across the load will be neglected.

When the transistor is switched off (marked as $t_{sw\text{-}off}$ in Figure 2), the current i_{LED}–i_{res} is positive and capacitor C_P starts charging. When its voltage reaches the bus voltage V_B, the clamping diode D_C turns on and the mosfet voltage is kept constant. When the current i_{LED}–i_{res} becomes negative, capacitor C_P is discharged until it reaches zero volts. At this point, the mosfet intrinsic diode starts conducting as it can be seen in the lower trace. The transistor must be switched on during this interval in order to obtain zero-voltage-switching (ZVS).

As it can be easily deduced from the circuit shown in Figure 1, when the clamping diode C_D is in the off-state, the current through the input source i_B is equal to the LED current. This allows sensing the load current using a simple resistor referred to ground placed in series with the input source. Adding a peak detector after this current sensor provides a cost-effective way to measure the load current even though it is not referred to ground.

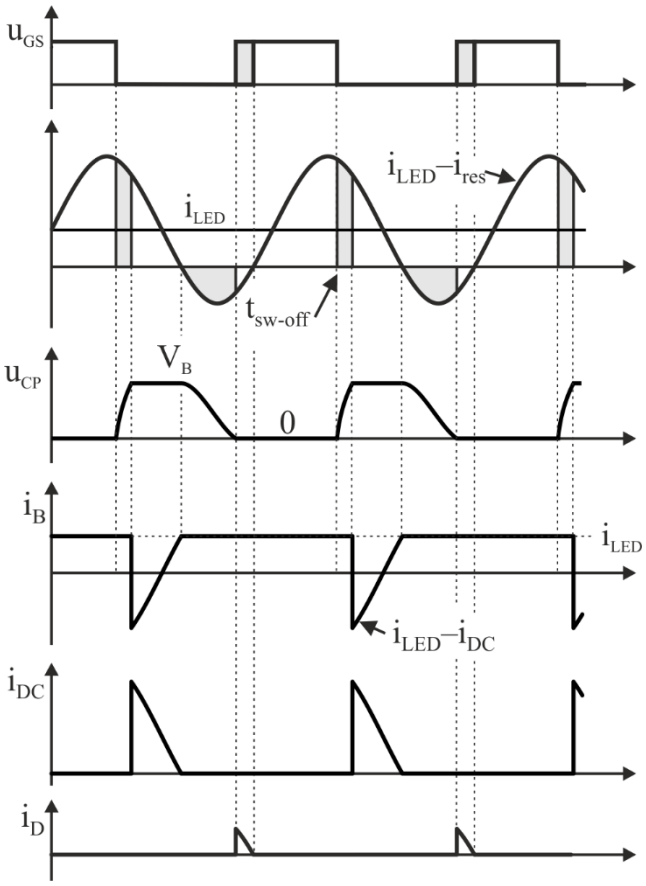

Figure 2. Circuit waveforms.

3. Static Analysis and Basic Design Equations

The design equations for the proposed circuit where explained in detail in [1]. The proposed procedure was based on selecting a suitable operating point at nominal power and then modifying the switching frequency in order to control the output power. In present work, this analysis will be revised and reoriented to determine how the operating point is modified when working at reduced power levels. As a first step, a brief review of the static behavior of the circuit will be made.

Considering the description made in the previous section, the circuit operation can be divided in four steps: charging of C_P, voltage clamped by D_C, discharge of C_P and voltage clamped at zero by the mosfet (or its intrinsic body diode D_{MOS}). Figure 3 shows these four steps and defines the angles where changes in the operating mode take place. According to this evolution, voltage C_P can be described by the following four interval equation:

$$U_{CP}(t) = \begin{cases} \frac{1}{C_P}\int_{\alpha/\omega}^{t}\left(i_{LED} - I_{res(peak)}\cdot\sin(\omega\cdot t_a)\right)\cdot dt_a & if \quad \frac{\alpha}{\omega} < t \le \frac{\beta}{\omega} \\ V_B & if \quad \frac{\beta}{\omega} < t \le \frac{asin(q)}{\omega} \\ V_B + \frac{1}{C_P}\int_{asin(q)/\omega}^{t}\left(i_{LED} - I_{res(peak)}\cdot\sin(\omega\cdot t_b)\right)\cdot dt_b & if \quad \frac{asin(q)}{\omega} < t \le \frac{\gamma}{\omega} \\ 0 & otherwise \end{cases}, \tag{1}$$

where ω is the angular frequency and $I_{res(peak)}$ is the peak value of the resonant current and parameter q is defined as:

$$q = \frac{i_{LED}}{I_{res(peak)}}. \tag{2}$$

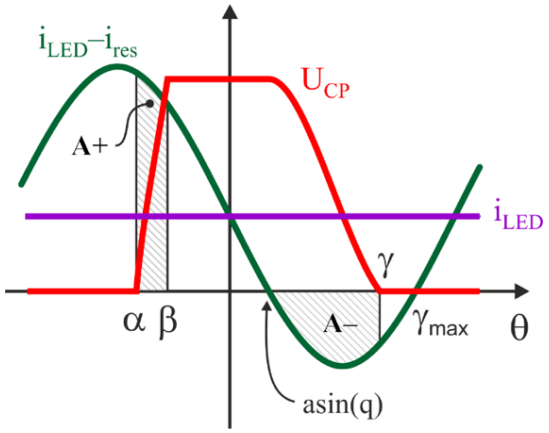

Figure 3. Detailed circuit waveforms and angle definitions.

Normalizing expression (1) it can be transformed into:

$$M_{CP}(\theta) = \begin{cases} \int_{\alpha}^{\theta} \left(1 - q^{-1}\sin(\theta_a)\right) \cdot d\theta_a & if \quad \alpha < \theta \leq \beta \\ M_B & if \quad \beta < \theta \leq asin(q) \\ M_B + \int_{asin(q)}^{\theta} \left(1 - q^{-1}\sin(\theta_b)\right) \cdot d\theta_b & if \quad asin(q) < \theta \leq \gamma \\ 0 & otherwise \end{cases}, \tag{3}$$

using the following definition:

$$U_{CP}(t) = \frac{I_{res(peak)}}{C_P \cdot \omega} M_{CP}(\omega \cdot t). \tag{4}$$

Besides, the normalized expression of the bus voltage M_B can be calculated by means of:

$$M_{B=} \int_{\alpha}^{\beta} \left(1 - q^{-1}\sin(\theta_a)\right) \cdot d\theta_a. \tag{5}$$

There are three equations that define the basic operating restrictions that apply to the proposed circuit. To define these equations the following additional parameter will also be used:

$$\kappa = \frac{V_B}{V_{LED}}. \tag{6}$$

The first equation comes from considering zero energy balance in capacitor C_P (A+ area equal to A- in Figure 3):

$$F1(q, \alpha, \beta, \gamma) = \beta - \alpha + \frac{1}{q}(cos(\beta) - cos(\alpha)) + \gamma - asin(q) + \frac{cos(\gamma) - \sqrt{1 - q^2}}{q} = 0. \tag{7}$$

An additional equation can be obtained considering that the input and output powers are equal:

$$F2(q, \beta, \kappa) = \frac{\kappa}{2\pi}\left(2\pi - asin(q) + \beta + \int_{\beta}^{asin(q)} \frac{1}{q} sin(\theta) \cdot d\theta\right) - 1 = 0, \tag{8}$$

As the resonant tank formed by L_R-C_R cannot handle active power, a third equation is obtained:

$$F3(q, \alpha, \beta, \gamma) = \int_{-\pi}^{\pi} M_{CP}(\theta, q, \alpha, \beta, \gamma) \cdot sin(\theta) \cdot d\theta = 0. \tag{9}$$

These three equations allow obtaining the angles α, β, γ and γ_{max} as a function of parameters q and κ. Figure 4 shows these angles as a function of q for three different κ values: 1.2, 1.6 and 2.

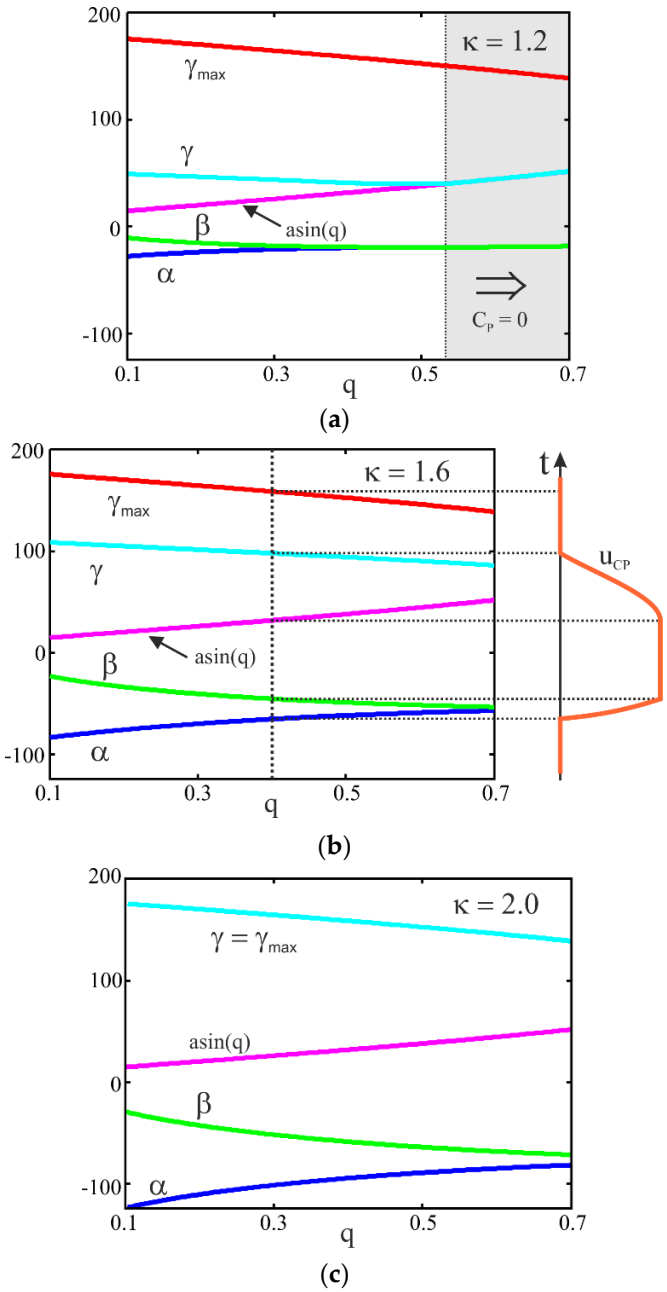

Figure 4. Variation of the angles α, β, *asin(q)*, γ and γ_{max} in degrees as a function of q for different k values: (**a**) k equal to 1.2; (**b**) k equal to 1.6; (**c**) k equal to 2.0.

For κ equal 2, angles γ and γ_{max} are equal and the circuit operates at the limit of ZVS. Figure 5 shows the converter waveforms in this particular case. To fulfill Equations (7)–(9), the only possibility is that the charging and discharging intervals of C_P have to be centered with respect to the minimum and maximum values of i_{res} current respectively. In this case, angles γ and γ_{max} are equal. Therefore, higher values of κ cannot be used in this circuit without severely reducing the efficiency.

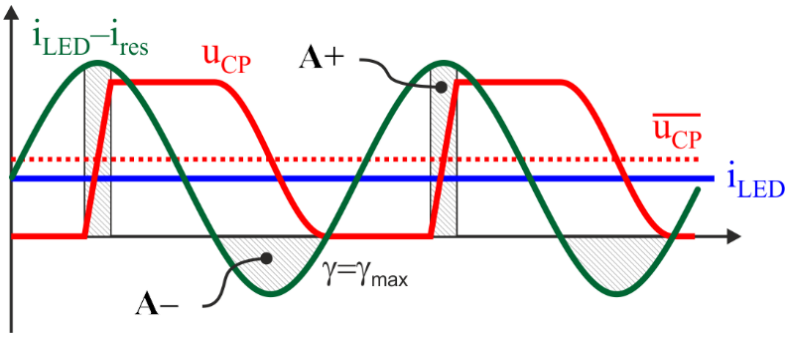

Figure 5. Theoretical waveforms for κ equal to 2.

To calculate the C_P value in [1], expression (1) was integrated between α and β providing the following equation:

$$\frac{{V_{LED}}^2}{P_{LED}} \cdot \omega \cdot C_P = \frac{1}{\kappa} \cdot \left(\beta - \alpha + q^{-1}(cos(\beta) - cos(\alpha))\right), \tag{10}$$

Besides, the fundamental component of the u_{CP} signal must be equal to the equivalent impedance of the resonant tank Z_{res} multiplied by the resonant current I_{res}:

$$\frac{V_B}{M_B} \cdot \frac{1}{\pi} \int_{-\pi}^{\pi} M_{CP}(\theta, q, \alpha, \beta, \gamma) \cdot cos(\theta) \cdot d\theta = Z_{res} \cdot I_{res(peak)}. \tag{11}$$

Combined with (5) and (6), expression (11) can be transformed in:

$$\frac{q \cdot \kappa \cdot \frac{1}{\pi} \int_{-\pi}^{\pi} M_{CP}(\theta, q, \alpha, \beta, \gamma) \cdot cos(\theta) \cdot d\theta}{\int_{\alpha}^{\beta} (1 - q^{-1} \sin(\theta_a)) \cdot d\theta_a} = \left|\omega \cdot L_R - \frac{1}{\omega \cdot C_R}\right| \cdot \frac{P_{LED}}{{V_{LED}}^2}. \tag{12}$$

Expressions (10) and (12) where used in [1] to calculate the values of the converter components (C_P, C_R and L_R), but they can also be combined with (7) to (9) to calculate how the LED power P_{LED} and the switching frequency ω are modified as a function of q and κ once the component values are known. Using the design parameters summarized on Table 1, the theoretical representation of i_{LED}, P_{LED} and $i_{res(peak)}$ as a function of the operating frequency where obtained. These relations are shown in Figure 6. The highlighted spot inside these graphics correspond to the nominal operating point. If the LED voltage and the bus voltage are kept constant, values will change following the traces with a constant κ.

As it can be seen, these three parameters present a strong dependence on the frequency thus providing a wide dimming range with a limited excursion of the control frequency. This is an interesting feature because it reduces the size of the electromagnetic interference (EMI) filter that will be required in a practical implementation [24].

To fully charge and discharge capacitor C_P the resonant current must be sufficiently high. However, at lower power levels, if the resonant current is high compared to the LED current (low q values), the losses in the resonant inductor will have a strong impact on the converter efficiency. Figure 6.c shows how the resonant current changes with the switching frequency. For a fixed load and bus voltages (κ equal to 1.6), the peak resonant current goes from 1.25 A at nominal power to 0.67 at 6W. This reduction in the resonant current at low LED currents contribute to maintain a good efficiency when the circuit works below its nominal operating power.

Special care has to be taken with the LED voltage reduction that takes place when working at low power levels. If the LED voltage is reduced or the bus voltage increases, the κ value will be higher thus increasing the risk of reaching the 2.0 limit and losing the ZVS condition. Fortunately, the voltage ripple of the power-factor-correction stage will be smaller at low power thus mitigating this effect.

Table 1. Design example specifications.

Basic Circuit Specifications			
Nominal input voltage 128 V Nominal output current 0.5 A	Input voltage excursion ±15 V (peak) Output voltage 80 ± 5 V		Nominal frequency 200 kHz Nominal output power 40 W
LED Lamp Characteristics			
Model Oslon SSL80	Manufacturer Osram	Nominal current 0.8 A	Number of LEDs 24
Parameters Chosen by Design			
q 0.4		κ 1.6	
Circuit Parameters			
C_P 3.7 nF L_R 141 µH ETD29 3F3	C_R 6.8 nF L_F 2 mH ETD29 3F3		Mosfet IRF640 Diode MUR120
Other Circuit Components Used in The Laboratory Prototype			
Microcontroller ARM STM32F407		Mosfet driver NCP87074A	

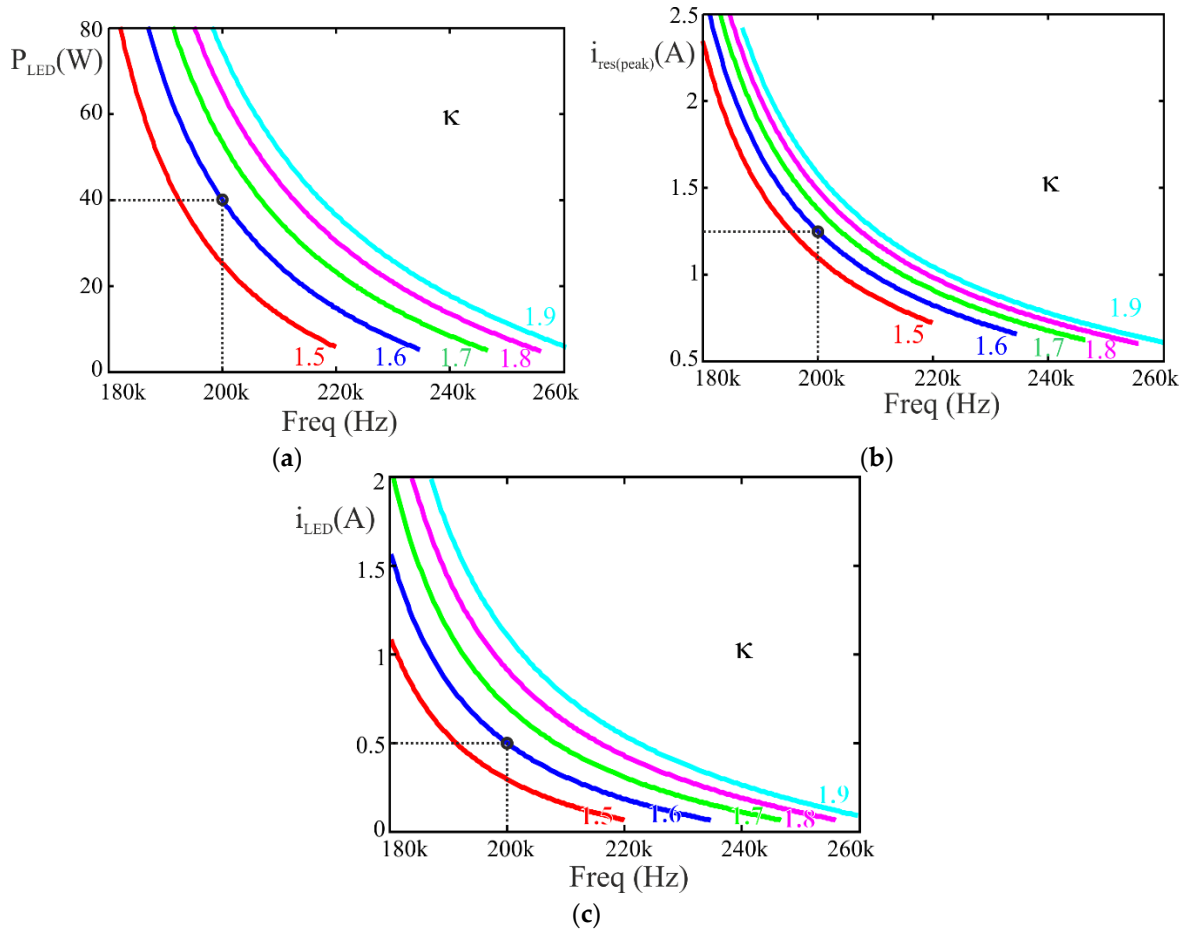

Figure 6. Theoretical evolution against changes in the operating frequency: (**a**) output power; (**b**) light-emitting diode (LED) current; (**c**) resonant current (peak value).

4. Simplified Small-Signal Dynamic Model

The linearization of the static model Equations (7)–(10) and (12) has been previously described by the authors in [1]. The small-signal static model can be expressed as:

$$\frac{\hat{i}_{LED}}{I_{LED0}} = H_{VB}(\omega_0, q_0, \alpha_0, \beta_0, \gamma_0, \kappa_0)\cdot\frac{\hat{V}_B}{V_{B0}} + H_{VLED}(\omega_0, q_0, \alpha_0, \beta_0, \gamma_0, \kappa_0)\cdot \frac{\hat{V}_{LED}}{V_{LED0}} + H_{\omega}(\omega_0, q_0, \alpha_0, \beta_0, \gamma_0, \kappa_0)\cdot\frac{\hat{\omega}}{\omega_0}. \tag{13}$$

This expression relates the quasi-static small-signal variations of the LED current $\hat{i}_{LED}$ with the small signal perturbations in the bus voltage $\hat{V}_B$, the LED voltage $\hat{V}_{LED}$ and the switching frequency $\hat{\omega}$. The terms H_{VB}, H_{VLED} and H_{ω} on previous expression can be calculated as functions of the steady state values of parameters: ω, q, α, β, γ and κ. Sub-index '0' will be used to identify steady state values.

To simplify the notation the following definitions will be used:

$$H_{VB0} = H_{VB}(\omega_0, q_0, \alpha_0, \beta_0, \gamma_0, \kappa_0), \tag{14}$$

$$H_{VLED0} = H_{VLED}(\omega_0, q_0, \alpha_0, \beta_0, \gamma_0, \kappa_0), \tag{15}$$

$$H_{\omega 0} = H_{\omega}(\omega_0, q_0, \alpha_0, \beta_0, \gamma_0, \kappa_0). \tag{16}$$

As it was made in the previous section, the small signal characteristic given by (13) can be calculated for a specific design as a function of ω and κ values. Using the parameters shown in Table 1, the sensitivity of the current $\hat{i}_{LED}$ against changes in the bus voltage $\hat{V}_B$, the LED voltage $\hat{V}_{LED}$ and the frequency $\hat{\omega}$ where calculated and the results obtained are shown in Figure 7. As it can be observed, the $\hat{i}_{LED}$ sensitivity against changes in $\hat{V}_B$ and $\hat{V}_{LED}$ signals increase significantly at higher frequencies (lower power levels). One of the consequences of this behavior is that, if a feedforward control is used to compensate for variations on the LED or the bus voltages, the gain of the controller must be changed depending on the dimming level.

As it was previously discussed, using the MFA technique with the proposed topology will lead to a fairly complex model. The approach that will be used in this work is based on the assumption that the dominant effect in the converter dynamics is given by the large value of inductor L_F. The purpose of this inductor is to obtain a small high-frequency current ripple across the LED thus the changes in the resonant components C_P, C_R and L_R will be significantly faster compared to those in the output current.

At the beginning of this section, the small-signal static expression of the LED current as a function of the bus and LED voltages and the switching frequency was obtained. Considering solely the variations on the LED voltage, Equation (13) can be written as:

$$\hat{i}_{LED}\cdot\frac{V_{LED0}}{I_{LED0}\cdot H_{VLED0}} = \hat{V}_{LED}. \tag{17}$$

Therefore, the small signal behavior of the LED current against small and quasi-static changes in the LED voltage can be defined by the following equivalent resistance:

$$R_{eq} = -\frac{V_{LED0}}{I_{LED0}\cdot H_{VLED0}}. \tag{18}$$

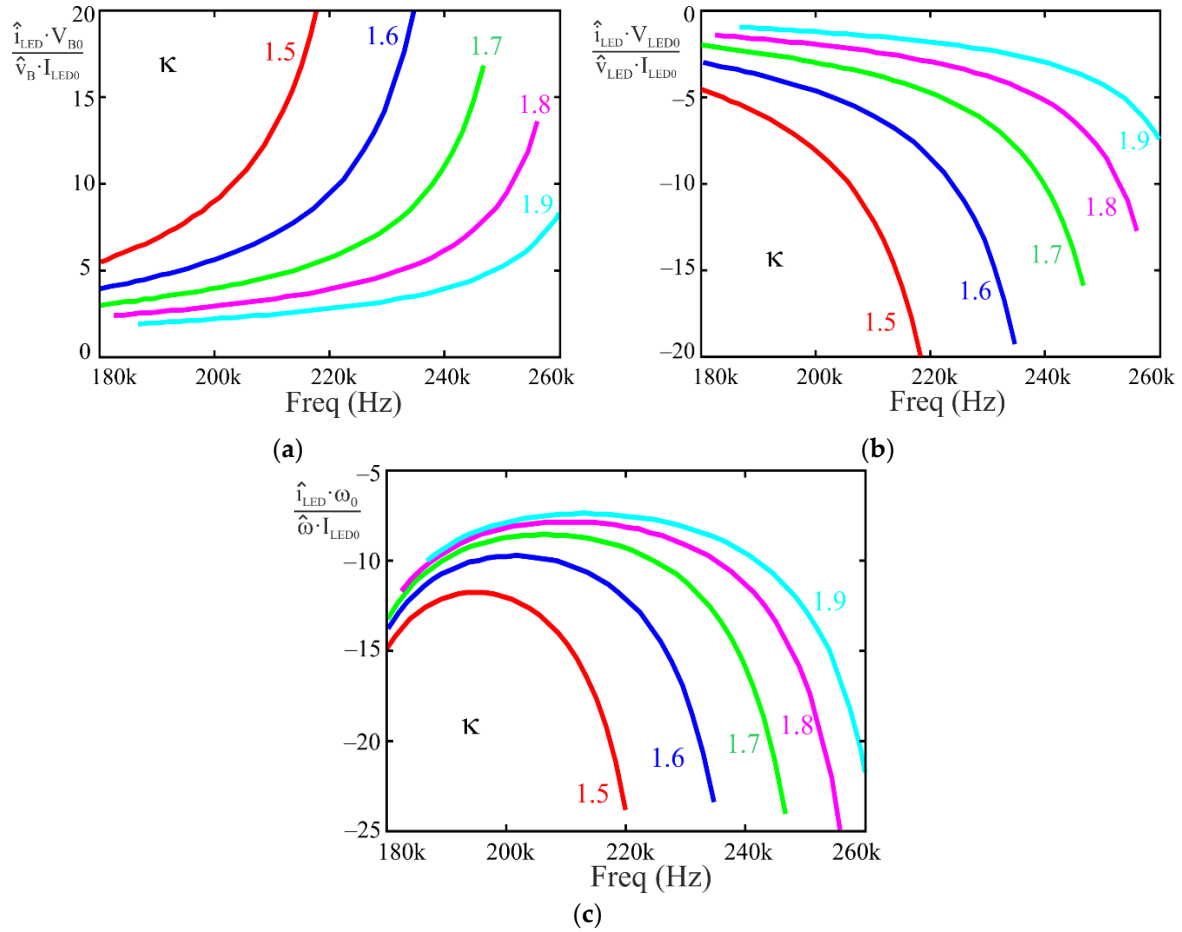

Figure 7. Sensitivity of LED current against changes in three different parameters as a function of the operating frequency: (**a**) Bus voltage; (**b**) LED voltage; (**c**) Frequency.

For a given operating point, this resistance can be calculated directly from Figure 7a. Therefore, if the dynamic of the circuit is determined by the filter inductance L_F, and any other effect can be considered instantaneous, the circuit shown in Figure 8 can be used to calculate the dynamic evolution of the LED current against changes in the LED voltage:

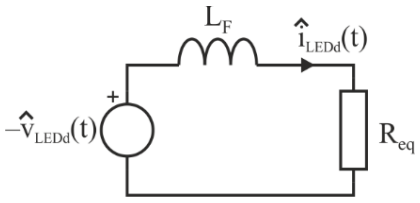

Figure 8. Small signal dynamic behavior approach.

Where $\hat{V}_{LEDd}(t)$ and $\hat{i}_{LEDd}(t)$ are the dynamic variations of the LED voltage and current respectively. This simplified equivalent predicts a first-order behavior in the circuit dynamics. The effect of the bus voltage and the frequency can also be included in the previous model with the same approach. Firstly, the quasi-static model given by Equation (13) will be rewritten using the definition (18) as:

$$-R_{eq}\cdot\hat{i}_{LED} = \hat{V}_{LED} + \frac{V_{LED0}\cdot H_{VB0}}{H_{VLED0}\cdot V_{B0}}\cdot\hat{V}_B + \frac{V_{LED0}\cdot H_{\omega 0}}{H_{VLED0}\cdot\omega_0}\cdot\hat{\omega}. \tag{19}$$

If the dynamic effect of the inductor L_F is included in this quasi-static model using the same approach as before the circuit in Figure 9 is obtained:

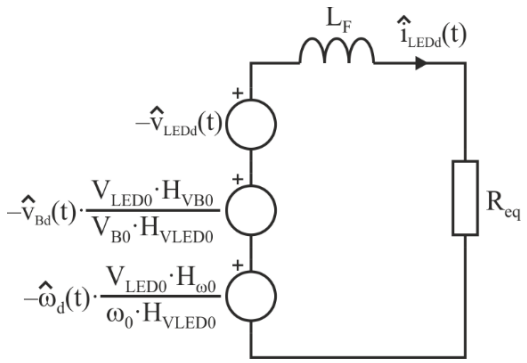

Figure 9. Small signal dynamic equivalent circuit.

This approach provides a single pole transfer function in the form:

$$\hat{i}_{LEDd}(s) = \frac{-1}{R_{eq}} \cdot \frac{1}{1+\frac{s}{\omega_P}} \cdot \hat{V}_{LED} + \frac{-1}{R_{eq}} \cdot \frac{V_{LED0} \cdot H_{VB0}}{H_{VLED0} \cdot V_{B0}} \cdot \frac{1}{1+\frac{s}{\omega_P}} \cdot \hat{V}_B + \frac{-1}{R_{eq}} \cdot \frac{V_{LED0} \cdot H_{\omega 0}}{H_{VLED0} \cdot \omega_0} \cdot \frac{1}{1+\frac{s}{\omega_P}} \cdot \hat{\omega}, \quad (20)$$

where ω_P is the system pole frequency:

$$\omega_P = \frac{R_{eq}}{L_F}. \quad (21)$$

Expression (21) can be calculated as a function of the frequency and κ values for a given design. Using the circuit parameters summarized in Table 1 the results shown in Figure 10 were obtained. As it can be seen, the system becomes faster at lower power levels.

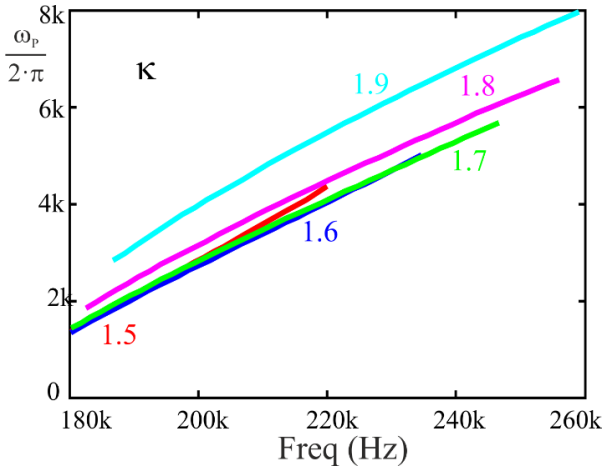

Figure 10. System pole frequency as a function of the operating frequency.

5. Feedback Loop Design

The feedback loop has to comply with two different goals: compensate the variations of the LED voltage and mitigate the strong effect that the bus voltage ripple has in the low-frequency LED light flicker. This last goal is required in order to comply with the IEEE PAR1789 recommendations. As in many resonant converters, the only parameter that can be used in this topology to control the load current is the switching frequency.

Considering that the dynamic behavior of the system corresponds to a single-pole transfer function, a simple PI regulator will be used for the control. Using Equation (20), the block diagram shown in Figure 11 is obtained.

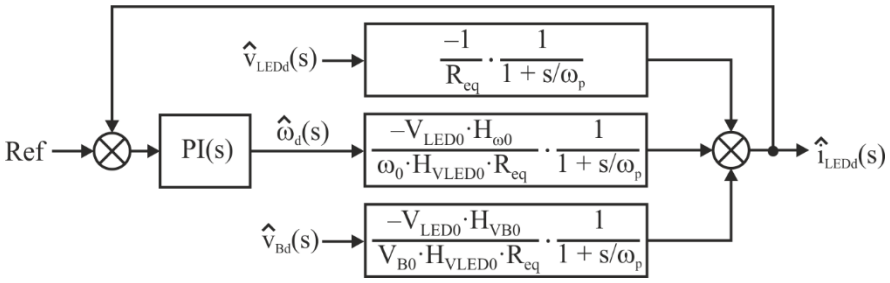

Figure 11. Small signal control loop.

Another aspect that must be considered is that the bus voltage ripple supplied by the PFC stage depends on the output power. For this analysis, the input stage will be assumed to work as an ideal resistance emulator with a constant power load (see Figure 12). Considering that the difference between the instantaneous input power P_B and the constant output power P_{OUT} must be handled by the bulk capacitor C_B, the energy balance in the capacitor can be expressed as:

$$\frac{1}{2} \cdot C_B \cdot V_{B(max)}{}^2 - \frac{1}{2} \cdot C_B \cdot V_{B(min)}{}^2 = A+, \tag{22}$$

where $A+$ is the positive shaded area in Figure 12b and C_B is the bulk capacitor placed at the output of the PFC stage. In this case, the peak-to-peak low frequency ripple can be estimated by the following formula:

$$V_{B(max)} - V_{B(min)} = \frac{P_{OUT}}{2 \cdot C_B \cdot \pi \cdot f_M \cdot \overline{V_B}}, \tag{23}$$

where f_M is the mains frequency and $\overline{V_B}$ is the average output voltage of the PFC. As it can be seen, if the input stage works as a constant voltage source, the output ripple is proportional to the output power. This characteristic helps to meet the flicker restrictions at reduced power levels. In this example, the C_B capacitor was 33 µF providing a peak-to-peak ripple of 30 V at nominal power for a mains frequency of 50 Hz.

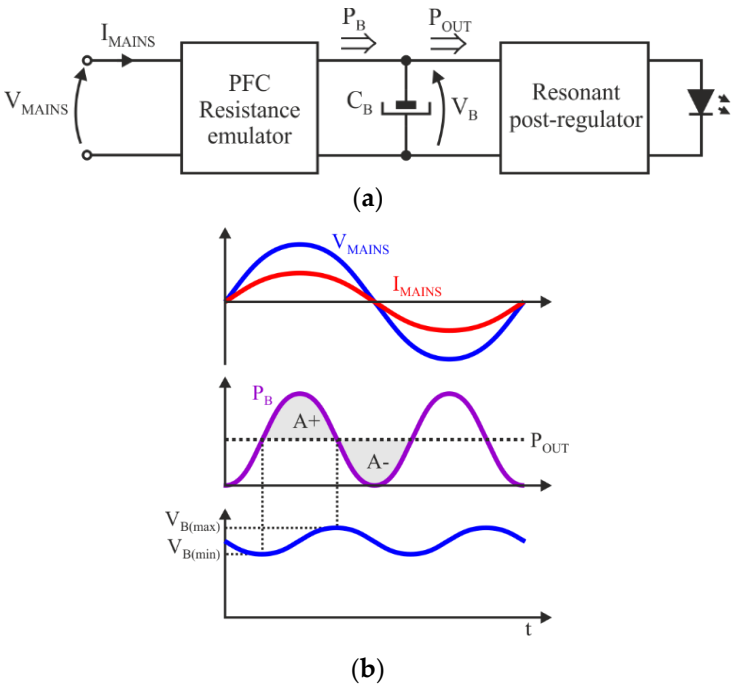

Figure 12. Input ripple estimation: (**a**) equivalent block diagram; (**b**) basic waveforms.

Therefore, considering that the worst conditions in terms of input voltage ripple will happen at maximum power, the PI controller will be designed to comply the low-frequency flicker constraint at the nominal operating point. After that, the fulfillment of this constraint and the stability margin will be verified inside the complete dimming range.

Table 2 summarizes the results obtained for the controller design. The zero of the controller was placed at the system pole frequency for a lamp voltage of 85.3V at nominal current, and the gain was calculated to obtain a low-frequency current ripple below 8%. The worst case to meet this condition was at minimum current and maximum lamp voltage. Ripple values were calculated according the definition used in the IEEE PAR1789 standard, that is:

$$Ripple(\%) = \frac{i_{LED(max)} - i_{LED(min)}}{i_{LED(max)} + i_{LED(min)}} \cdot 100. \tag{24}$$

Table 2. Controller design.

System Model		
$\frac{-1}{R_{eq}} \cdot \frac{1}{1+\frac{s}{\omega_P}}$	$\frac{-V_{LED0} \cdot H_{VB0}}{R_{eq} \cdot H_{VLED0} \cdot V_{B0}} \cdot \frac{1}{1+\frac{s}{\omega_P}}$	$\frac{-V_{LED0} \cdot H_{\omega 0}}{R_{eq} \cdot H_{VLED0} \cdot \omega_0} \cdot \frac{1}{1+\frac{s}{\omega_P}}$
V_{LED} = 75 V I_{LED} = 0.53 A		
$\frac{-0.024}{1+\frac{s}{2.04 \cdot 10^4}}$	$\frac{0.018}{1+\frac{s}{2.04 \cdot 10^4}}$	$\frac{-2.19 \cdot 10^{-5}}{1+\frac{s}{2.04 \cdot 10^4}}$
V_{LED} = 85.3 V I_{LED} = 0.53 A		
$\frac{-0.037}{1+\frac{s}{1.35 \cdot 10^4}}$	$\frac{0.029}{1+\frac{s}{1.35 \cdot 10^4}}$	$\frac{-3.34 \cdot 10^{-5}}{1+\frac{s}{1.35 \cdot 10^4}}$
V_{LED} = 75 V I_{LED} = 0.14 A		
$\frac{-0.016}{1+\frac{s}{3.17 \cdot 10^4}}$	$\frac{0.01}{1+\frac{s}{3.17 \cdot 10^4}}$	$\frac{-8.07 \cdot 10^{-6}}{1+\frac{s}{3.17 \cdot 10^4}}$
V_{LED} = 85.3 V I_{LED} = 0.14 A		
$\frac{-0.022}{1+\frac{s}{2.34 \cdot 10^4}}$	$\frac{0.016}{1+\frac{s}{2.34 \cdot 10^4}}$	$\frac{-9.1 \cdot 10^{-6}}{1+\frac{s}{2.34 \cdot 10^4}}$
PI Controller		
$500 \cdot 10^6 \cdot \frac{1+\frac{s}{1.35 \cdot 10^4}}{s}$		
Output Current Flicker at 100 Hz		
I_{LED} = 0.53 A		I_{LED} = 0.14 A
V_{LED} = 75 V	V_{LED} = 85.3 V	V_{LED} = 75 V	V_{LED} = 85.3 V
2.9%	3.5%	4.5%	7.1%
Digital Controller		
Sampling frequency	Antialiasing filter	PI transfer function
10 kHz	$\frac{1}{1+\frac{s}{2.6 \cdot 10^4}}$	$\frac{5.62 \cdot 10^4 - 6.19 \cdot 10^3 \cdot z^{-1}}{1-z^{-1}}$

For the practical implementation of the controller a digital regulator was used. The 'z' transfer function was calculated using the bilinear transform with a sampling frequency of 10 kHz. A first-order antialiasing filter with a corner frequency of 4.1 kHz was used in the experimental setup.

Figure 13 shows the Bode plot of the loop gain for a lamp voltage of 75 V and 85.3 V with a LED current of 0.53 A and 0.14 A. As it can be seen, the stability condition is met for the proposed design. This loop gain corresponds to the product of three transfer functions: system model, PI controller and antialiasing filter. These transfer functions are shown in Table 2.

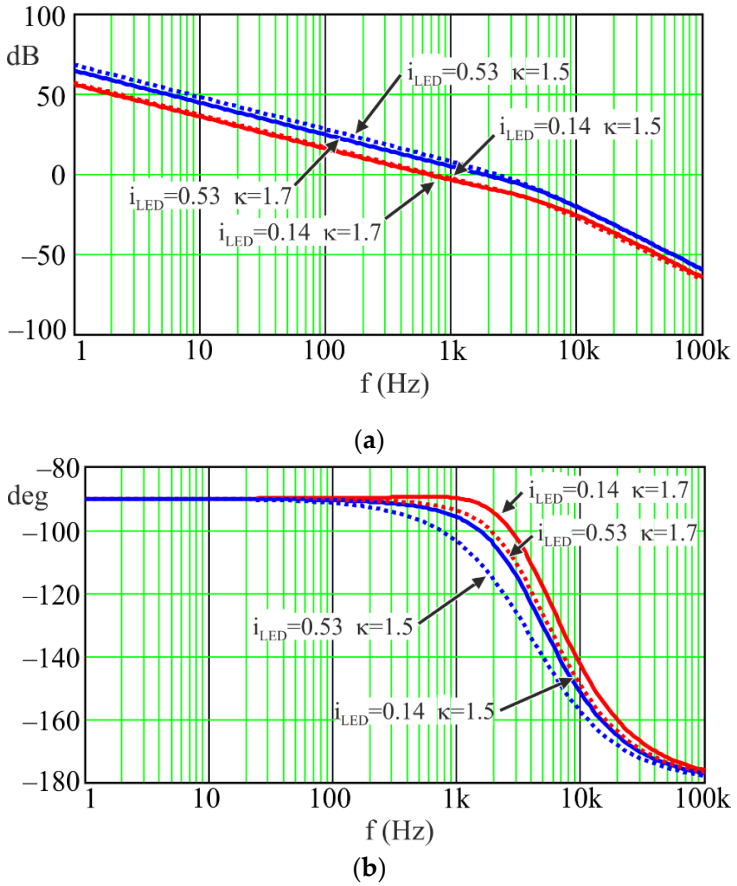

Figure 13. Bode plot of the loop gain: (**a**) gain modulus; (**b**) gain phase.

According to the previous analysis, the design methodology for the resonant converter and the PI regulator can be schematized as seen in Figure 14. The first step of the design is calculating the circuit parameters at nominal power. This step, including the design charts and the specific criteria to optimize the operation at nominal power, was thoroughly described in Reference [1]. The proposed procedure is based on the static analysis described in Section 3 and it provides the values for the main circuit components of the power topology (C_P, L_R, C_R and L_F).

The second step of the design is calculating how the operating point is modified during dimming. The frequency excursion required to obtain the desired output power control range can be calculated using the procedure described in Section 3. If this excursion is not valid for a specific application, the design of the nominal operating point must be adjusted accordingly.

The third step of the design methodology described in Figure 14 is estimating the input voltage ripple provided by the PFC stage. In the case that this stage behaves as an ideal resistance emulator, the converter input ripple can be calculated as a function of the output power using expression (23).

After this step, the parameters of the small signal model of the resonant converter must be calculated according to the methodology described in Section 4. These parameters will change with the output power.

The last step of the design is calculating the PI regulator parameters to ensure stable operation while complying with the flicker recommendations of IEEE PAR1789. As the dynamic behavior of the converter corresponds with a single-pole stable transfer function, a simple PI controller will normally suffice to ensure a stable operation in all dimming range.

The higher gain that the system has at low power levels (see Figure 7b) increases the effect of the input ripple but, according with expression (23), the actual input voltage ripple provided by the PFC

stage is also smaller thus the condition given by expression (24) must be verified both at nominal and minimum lamp power.

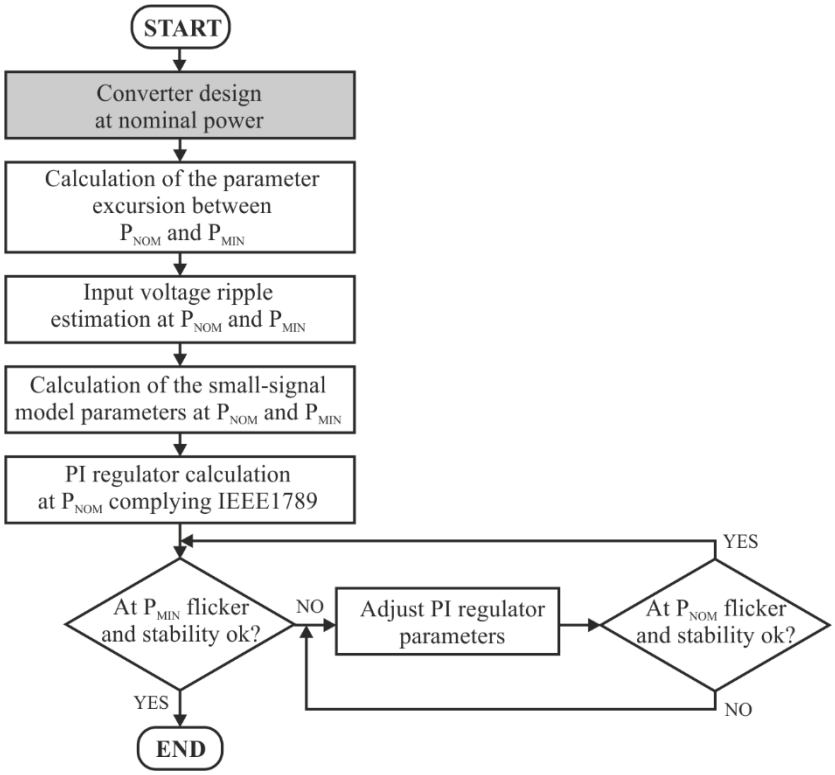

Figure 14. Proposed design methodology.

6. Simulation Results

To verify the proposed simplified model and the behavior of the controller the circuit was simulated using PSIM 9.0 Software. This software works with a fixed simulation time-step and it is especially suited to simulate power converters were the semiconductor transient behavior is not critical. It also allows the implementation of complex control strategies in a straightforward way.

The circuit implemented in the simulation was the one shown in Figure 1 with the component values in Table 1. The control block included an enable signal to select whether the circuit operates at constant frequency or with the PI regulator described in previous section. The turn-on of the switch was made either when the MOSFET voltage falls below a threshold value or when the duty cycle is lower than a minimum value of 20%. This behavior is required in the converter start-up transient.

The first simulation was used to check the validity of the simplified small-signal model proposed in Section 4 (see Figure 9). To do so, both the complete converter and the simplified model were simulated with 2.5% step changes in bus voltage, LED voltage and frequency. Figure 15a shows the results obtained at nominal LED current for a switching frequency of 203.2 kHz. In the same way, and for a LED current of 0.14A, another step transient simulation was carried out and the results are shown in Figure 15b. As it can be seen in both simulations, although the simulation confirmed the first-order behavior, the gain predicted by the model for small-signal steps in the bus and LED voltages is slightly higher compared to the actual results. The concordance in the case of small frequency steps is significantly better.

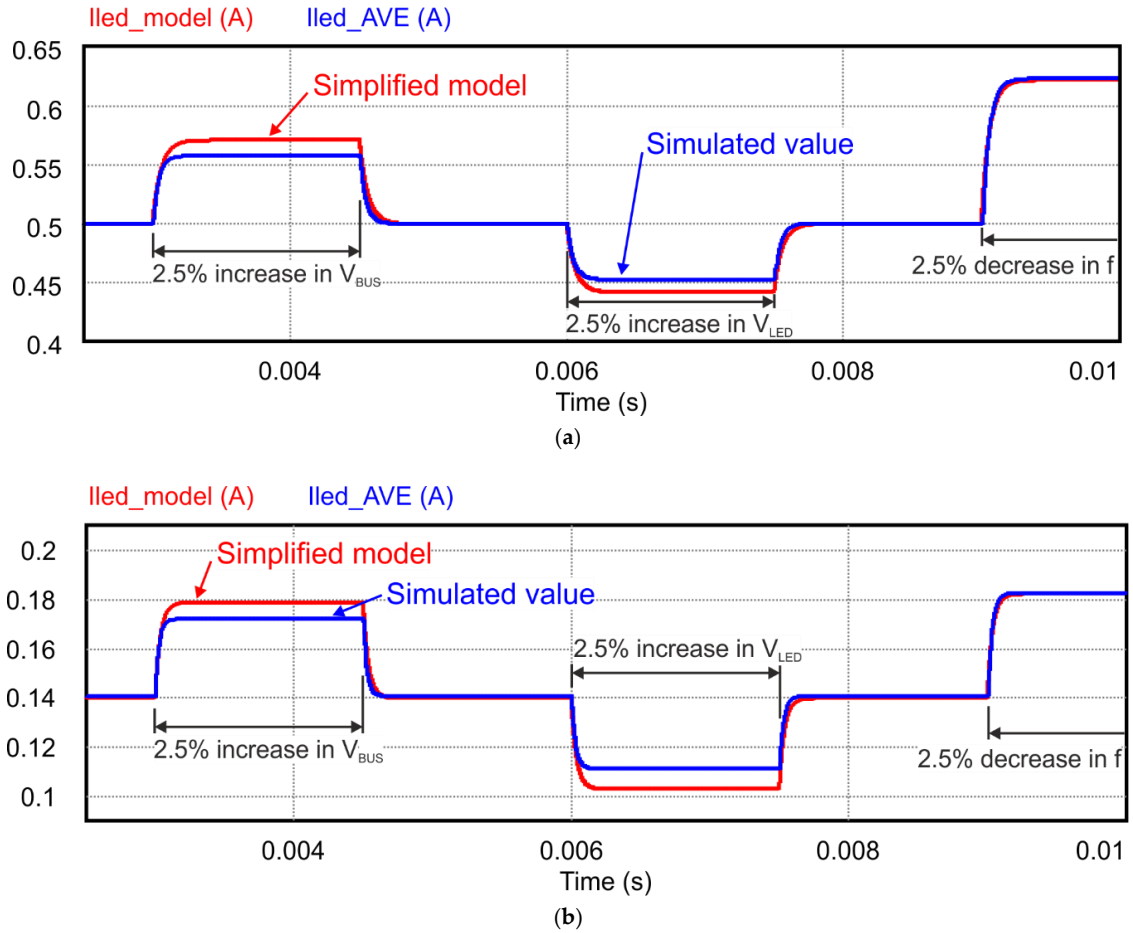

Figure 15. Simulated open-loop step-response of the actual average LED current (blue) and the proposed simplified model (red): (**a**) at nominal power; (**b**) for i_{LED} equal to 0.14A.

Figure 16 shows the LED current ripple with and without the PI controller enabled at two different dimming levels. The bus voltage input ripple was modified linearly with the converter output power according to expression (22). In both cases, and with the PI controller enabled, the LED ripple was below 8% required by the IEEE PAR1789 standard. The stair-like evolution that can be seen in the frequency signal is due to the 10 kHz equivalent sampling frequency used for the simulation.

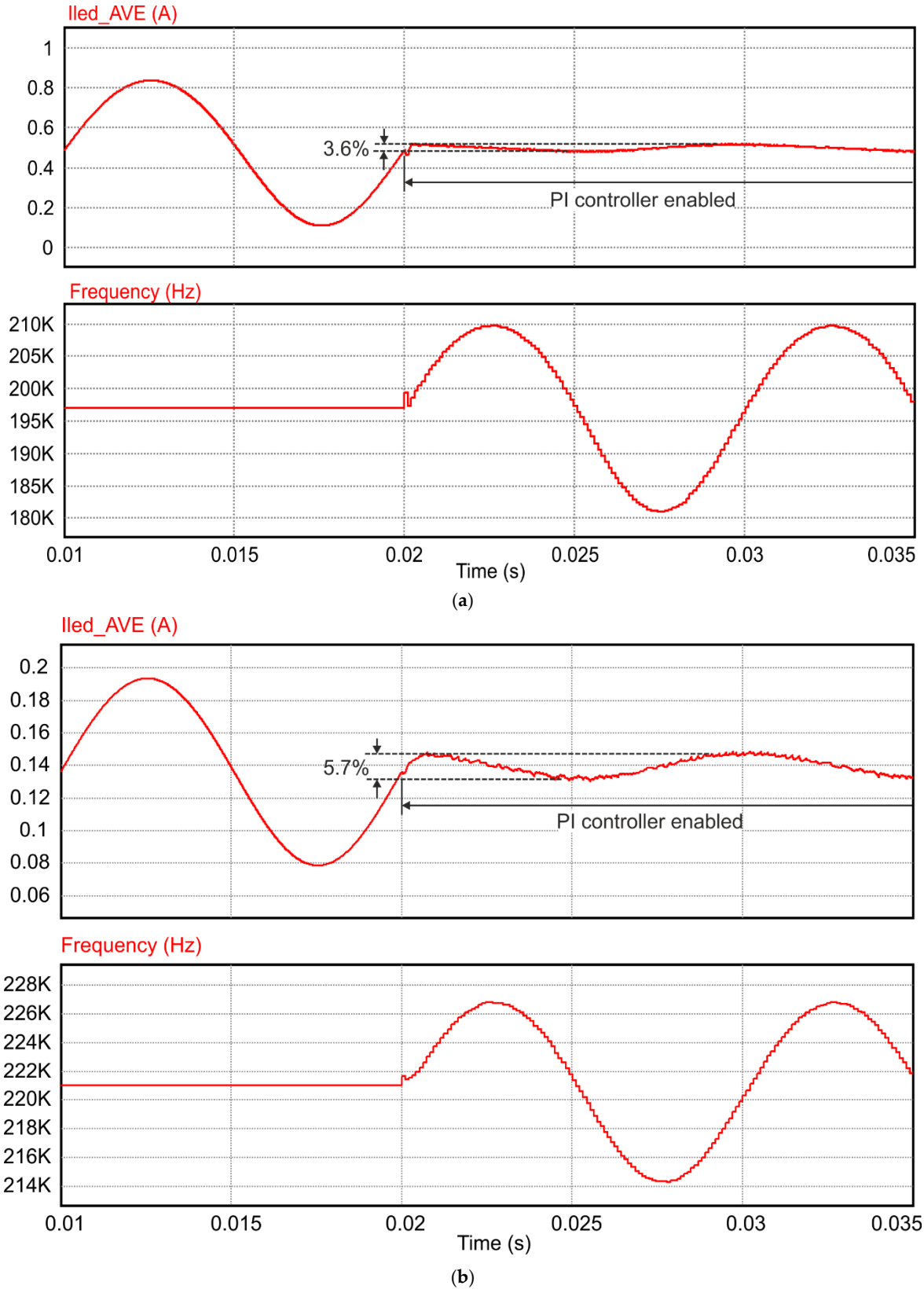

Figure 16. Simulated closed loop LED current ripple and frequency for $V_{BUS} = 128 \pm 4.2$ V, $V_{LED} = 85.3$ V: (**a**) for $i_{LED} = 0.5$ A, (**b**) for $i_{LED} = 0.14$ A.

7. Experimental Results

To further verify the behavior of the proposed power topology and control, a laboratory prototype was built based on the specifications in Table 1. A photograph of the prototype is shown in Figure 17. To emulate the behavior of the power factor correction stage an AC source model Agilent HP681B was used. This source allows to obtain a DC signal with a controllable AC ripple. The load was built using 24 SSL80 white LEDs from Osram connected in series. This lamp provides a voltage that varies between 85.3 and 75 volts when the output power is adjusted between 45 and 10 watts.

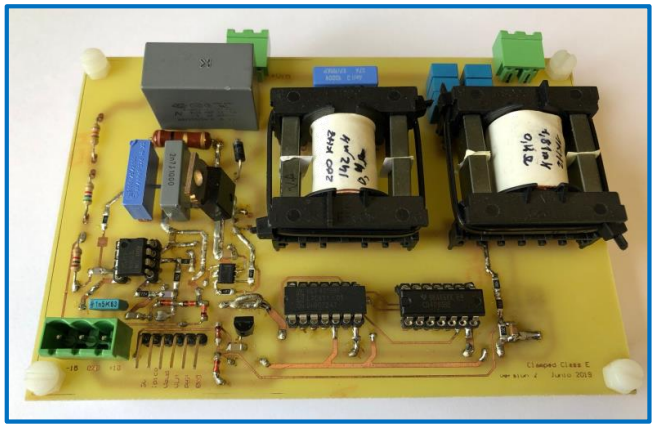

Figure 17. Laboratory prototype.

To measure the LED current, an Agilent JP48100658 current probe was used. The load voltage was measured using a Yokogawa 700924 differential probe. Input and output powers were measured using a Yokogawa WT3000 Precision Power Analyzer.

The first experiment conducted was made to verify the simplified dynamic model proposed in this work. For this purpose, the converter was tested in open loop configuration using a frequency modulated control signal obtained using a function generator model Agilent 33210A. The frequency excursion was set to ±2 kHz and the modulation frequency was modified from 100 Hz to 10 kHz. Figure 18 shows the ratio between the small-signal variation of the LED current and the amplitude of the frequency excursion in decibels. The continuous red trace represents the expected evolution according the simplified model. The blue crosses are the actual values measured in the prototype. However, the theoretical evolution was calculated assuming a constant LED voltage. If the LED voltage ripple is measured and this ripple is compensated according the theoretical gain between $\hat{\imath}_{LED}$ and $\hat{v}_{LED}$, the corrected values marked with red crosses in the figure are obtained. As it can be seen, the corner frequency predicted by the model is in good agreement with the measured value.

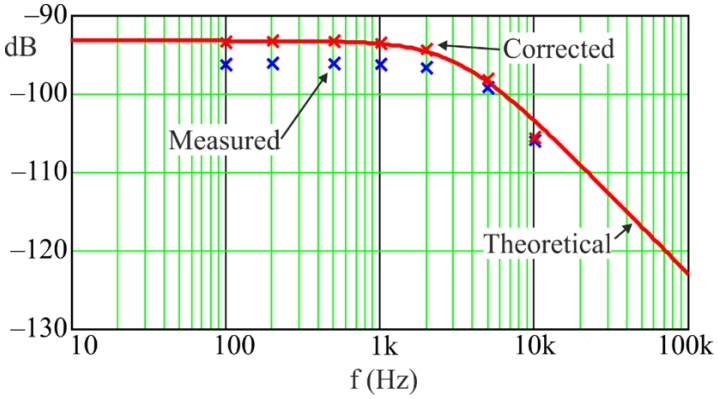

Figure 18. Theoretical and experimental LED current small-signal response against changes in the operating frequency.

The HP681B AC source used to supply the converter only allowed to introduce AC components up to 1 kHz thus the effect of $\hat{V}_B$ could not be experimentally verified this setup.

Figure 19 shows the simplified schematic of the circuit used for experimentation. The LED current is measured indirectly by sensing the current supplied by the input source. As it was already explained in Section 2, when the clamping diode is in the off-state, the LED current and the source current will be equal. On the other hand, when the clamping diode is on, the current through the source will be lower thus a peak detector that captures the maximum current handled by the source during a switching cycle will provide the LED current. Two Schottky diodes were used to reduce the power dissipated in the sensing resistor R_{PS}. The comparator and the synchronization block were used to switch on the transistor just after the capacitor C_P is fully discharged.

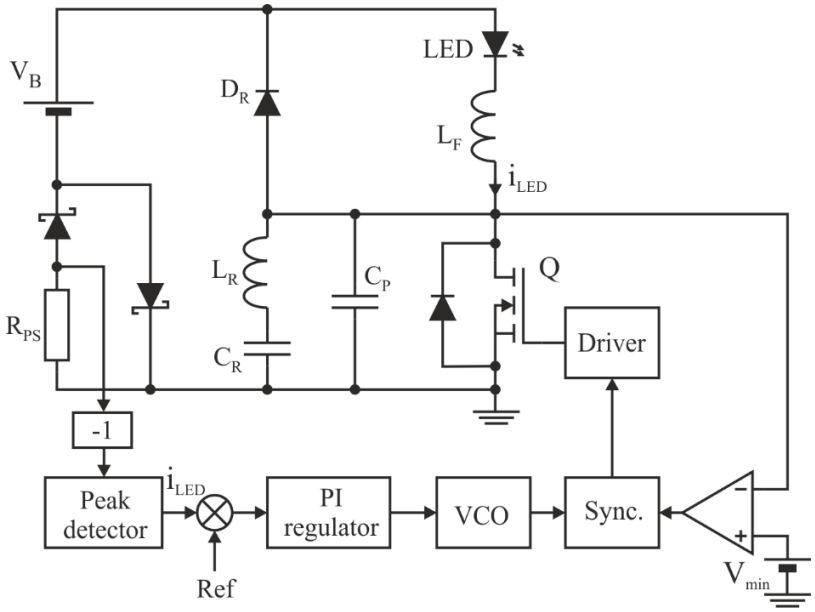

Figure 19. Simplified schematic of the control circuit.

For the practical implementation of the control circuit, the PI regulator and the voltage-controlled oscillator (VCO) blocks shown in Figure 19 were built using an ARM STM32F407 low-cost microcontroller. This microcontroller was used to implement the digital controller described in Section 5, whose transfer function is included in Table 2.

In the practical implementation of the circuit, the maximum and minimum frequencies were limited to 150 and 250 kHz respectively and the maximum frequency variation between samples was limited to 3 kHz. This last protection is only required when steep changes take place, such as the starting transient of the converter.

Figures 20 and 21 show the experimental waveforms of i_{LED}, v_{LED} and v_{BUS} measured at two different power levels with the PI controller enabled. The first was obtained for a LED current of 0.5 A and 15 V peak bus voltage ripple, and the second was obtained for 0.14 A and 4.2 V ripple according to expression (23). As it can be observed on both figures, the ripple limit is below the maximum 8% limit imposed by the IEEE PAR1789 standard.

One of the most critical concerns in the proposed design procedure is complying with the ripple restrictions set in Reference [11]. The ripple values calculated using the procedure described in Section 5 are summarized in Table 3 together with the results obtained by simulation and those experimentally measured. As it can be observed, the experimental values are slightly higher than both simulated and calculated ones, probably due to the noise induced in the LED current sensing circuitry. The deviation between the calculated and simulated ripple at low current is due to the high sensitivity the converter has while working at low power levels.

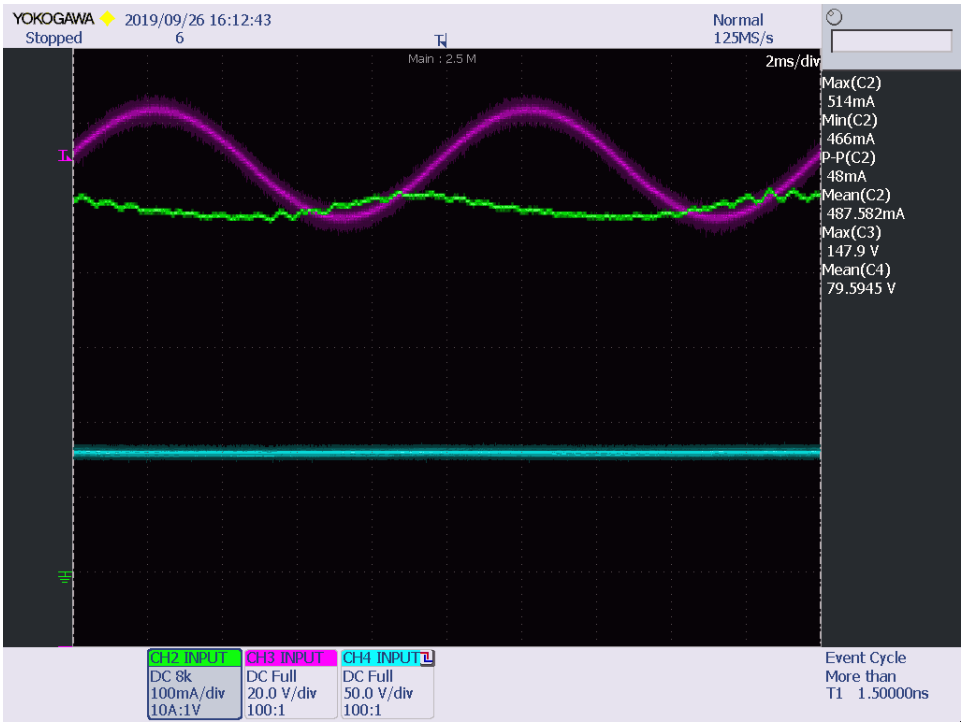

Figure 20. Experimental waveforms at nominal power with PI controller enabled. (4.9% ripple). Channel 2: LED current, green trace, 0.1 A/div; Channel 3: Bus voltage, magenta trace, 20 V/div; Channel 4: LED voltage, cyan trace, 50 V/div.

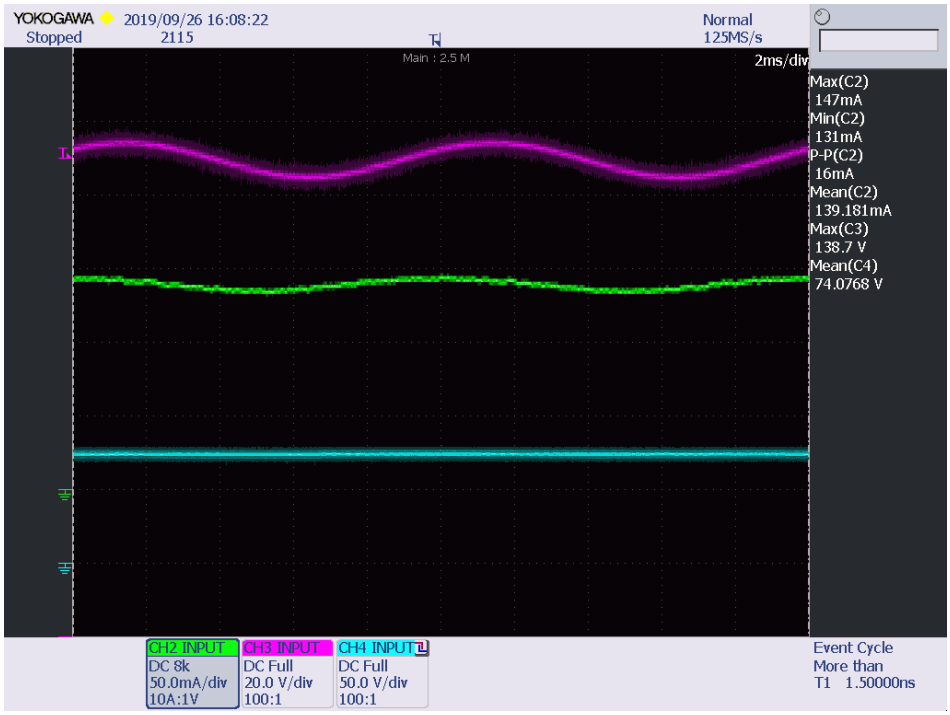

Figure 21. Experimental waveforms at i_{LED} = 0.14 A with PI controller enabled. (5,7% ripple). Channel 2: LED current, green trace, 50 mA/div; Channel 3: Bus voltage, magenta trace, 20 V/div; Channel 4: LED voltage, cyan trace, 50 V/div.

Table 3. Comparison between calculated, simulated and experimental LED current ripples.

Output Current Flicker at 100 Hz			
Calculated			
I_{LED} = 0.53 A		I_{LED} = 0.14 A	
V_{LED} = 75 V	V_{LED} = 85.3 V	V_{LED} = 75 V	V_{LED} = 85.3 V
2.9%	3.5%	4.5%	7.1%
Simulated			
I_{LED} = 0.53 A		I_{LED} = 0.14 A	
V_{LED} = 75 V	V_{LED} = 85.3 V	V_{LED} = 75 V	V_{LED} = 85.3 V
2.6%	3.6%	3.6%	5.7%
Experimental			
I_{LED} = 0.53A V_{LED} = 85.3V		I_{LED} = 0.14A V_{LED} = 75 V	
4.9%		5.7%	

8. Conclusions

The present work complements the results presented by the authors in [1]. In this previous work, the circuit was controlled using a feedforward control. This alternative has two important drawbacks: it cannot be used to compensate deviations on the component values and the feedforward gain must be adapted to the dimming level in order to comply with the flicker constraints of IEEE 1789. In the present work, a new control scheme based on implementing a feedback control loop to control the LED current has been proposed. Although the LED is not referred to ground, its current can be sensed indirectly by adding a shunt resistance in series with the input source. This shunt combined with a peak detector provides a low-cost alternative to measure the load current.

To analyze the small-signal dynamic behavior of the resonant converter, a simplified first-order model has been proposed. The simplification used to derive this model is based on the fact that the dominant dynamic is given by the filter inductance placed in series with the LED.

This model was used to calculate the small-signal system transfer function at different power levels and lamp voltages. These results were used to calculate a simple PI regulator to ensure the compliance of the LED current ripple condition while maintaining system stability.

The model and the controller were also tested using PSIM 9.0 simulation software and experimentally using a laboratory prototype. The results obtained were in good agreement with the expected values.

Author Contributions: Conceptualization, J.R.; writing—original draft preparation, J.R.; methodology, P.J.Q.; writing—review and editing, J.C. and P.J.Q.; validation, A.J.C.; supervision, J.M.L.; funding acquisition, J.M.L. and A.J.C.

Funding: This research received no external funding.

Conflicts of Interest: The authors declare no conflict of interest.

References

1. Ribas, J.; Quintana, P.J.; Cardesin, J.; Calleja, A.J. Lopez-Corominas, E.; Single-Switch LED Post-Regulator Based on a Modified Class-E Resonant Converter with Voltage Clamp. *Electronics* **2019**, *8*, 798. [CrossRef]
2. Rubinstein, F.; Siminovitch, M.; Verderber, R. Fifty Percent Energy Savings with Automatic Lighting Controls. *IEEE Trans. Ind. Appl.* **1993**, *29*, 768–773. [CrossRef]
3. Lee, H.; Choi, C.; Sung, M. Development of a Dimming Lighting Control System Using General Illumination and Location-Awareness Technology. *Energies* **2018**, *11*, 2999. [CrossRef]
4. Hermoso-Orzaez, M.J.; Lozano-Miralles, J.A.; Lopez-Garcia, R.; Brito, P. Environmental Criteria for Assessing the Competitiveness of Public Tenders with the Replacement of Large-Scale LEDs in the Outdoor Lighting of Cities as a Key Element for Sustainable Development: Case Study Applied with PROMETHEE Methodology. *Sustainability* **2019**, *11*, 5982. [CrossRef]

5. Pandharipande, A.; Newsham, G.R. Lighting controls: Evolution and revolution. *Light. Res. Technol.* **2018**, *50*, 115–128. [CrossRef]
6. Carli, R.; Dotoli, M.; Cianci, E. An Optimization Tool for Energy Efficiency of Street Lighting Systems in Smart Cities. *IFAC PapersOnLine* **2017**, *50*, 14460–14464. [CrossRef]
7. Pandharipande, A.; Caicedo, D. Smart Indoor Lighting Systems with Luminaire-Based Sensing: A Review of Lighting Control Approaches. *Energy Build.* **2015**, *104*, 369–377. [CrossRef]
8. Ashibe, M.; Miki, M.; Hiroyasu, T. Distributed optimization algorithm for lighting color control using chroma sensors. In Proceedings of the 2008 IEEE International Conference on Systems, Man and Cybernetics, Singapore, 12–15 October 2008. [CrossRef]
9. Dyble, M.; Narendran, N.; Bierman, A.; Klein, T. Impact of Dimming White LEDs: Chromaticity Shifts Due to Different Dimming Methods. In Proceedings of the SPIE-The International Society for Optical Engineering, San Diego, CA, USA, 14 September 2005; pp. 291–299. [CrossRef]
10. Vaitonis, Z.; Stonkus, A.; Žukauskas, A. Effect of Junction Temperature Oscillation on Output Characteristics of a Light-Emitting Diode under Pulse-Width and Pulse-Frequency Modulation Driving Modes. *IET Optoelectron.* **2012**, *6*, 52–56. [CrossRef]
11. IEEE Standards Association. *IEEE PAR1789: Recommended Practices for Modulating Current in High Brightness LEDs for Mitigating Health Risks to Viewers*; IEEE Standards: Piscataway, NJ, USA, 2015. [CrossRef]
12. Polin, D.; Klir, S.; Wagner, M.; Khanh, T.Q. Reducing the Stroboscopic Effects of LED Luminaires with Pulse Width Modulation Control. *Light. Res. Technol.* **2016**, *49*, 370–380. [CrossRef]
13. Zhang, F.; Xu, J. A Novel PCCM Boost PFC Converter with Fast Dynamic Response. *IEEE Trans. Ind. Electron.* **2011**, *58*, 4207–4216. [CrossRef]
14. Chen, Z.; Zhang, C.; Wu, Y.; Chen, Y.; Zhang, C. Series-Capacitor-Based Buck PFC Converter With High Power Factor and Ultrahigh Step-Down Conversion Ratio. *IEEE Trans. Ind. Electron.* **2019**, *66*, 6895–6905. [CrossRef]
15. Dong, H.; Xie, X.; Jiang, L.; Jin, Z.; Zhao, X. An Electrolytic Capacitor-Less High Power Factor LED Driver Based on a "One-and-a-Half Stage" Forward-Flyback Topology. *IEEE Trans. Power Electron.* **2018**, *33*, 1572–1584. [CrossRef]
16. Zhang, J.; Jiang, T.; Wu, X. A High-efficiency Quasi-two-stage LED Driver with Multi-channel Outputs. *IEEE Trans. Ind. Electron.* **2017**, *64*, 5875–5882. [CrossRef]
17. Moon, S.C.; Koo, G.B.; Moon, G.W. An Interleaved Single-Stage Flyback AC-DC Converter with Wide Output Power Range for Outdoor LED Lighting System. In Proceedings of the Twenty-Seventh Annual IEEE Applied Power Electronics Conference and Exposition, Orlando, FL, USA, 5–9 February 2012; pp. 823–830. [CrossRef]
18. Wang, Y.; Guan, Y.; Xu, D.; Wang, W. A CLCL Resonant DC/DC Converter for Two-Stage LED Driver System. *IEEE Trans. Ind. Electron.* **2015**, *63*, 2883–2891. [CrossRef]
19. Choi, S.; Kim, T. Symmetric Current-Balancing Circuit for LED Backlight With Dimming. *IEEE Trans. Ind. Electron.* **2012**, *59*, 1698–1707. [CrossRef]
20. Sanders, S.R.; Noworolski, J.M.; Liu, X.Z.; Verghese, G.C. Generalized averaging method for power conversion circuits. *IEEE Trans. Power Electron.* **1991**, *6*, 251–259. [CrossRef]
21. Bernal, C.; Oyarbide, E.; Molina, P.; Mediano, A. Dynamic Model of Class-E Inverter with Multifrequency Averaged Analysis. *IEEE Trans. Ind. Electron.* **2012**, *59*, 3737–3744. [CrossRef]
22. Ribas, J.; Alonso, J.M.; Lopez-Corominas, E.; Cardesin, J.; Rodríguez, F.; Garcia-Garcia, J.; Rico-Secades, M.; Calleja, A.J. Analysis of lamp-ballast interaction using the multi-frequency-averaging technique. In Proceedings of the 2001 IEEE 32nd Annual Power Electronics Specialists Conference, Vancouver, BC, Canada, 17–21 June 2001. [CrossRef]
23. Middlebrook, R.; Cuk, S. A General Unified Approach to Modeling Switching-Converter Power Stages. *Int. J. Electron. Theor. Exp.* **1977**, *42*, 521–550. [CrossRef]
24. Giglia, G.; Ala, G.; Di Piazza, M.C.; Giaconia, G.C.; Luna, M.; Vitale, G.; Zanchetta, P. Automatic EMI Filter Design for Power Electronic Converters Oriented to High Power Density. *Electronics* **2018**, *7*, 9. [CrossRef]